Article

Research on Reactive Power Optimization Control of a Series-Resonant Dual-Active-Bridge Converter

Junjuan Wu, Wei Zhang, Xiaofeng Sun * and Xinyu Su

Key Lab of Power Electronics for Energy Conservation and Motor Drive of Hebei Province, Yanshan University, Qinhuangdao 066004, China; wujunjuan@ysu.edu.cn (J.W.); zw1009@stumail.ysu.edu.cn (W.Z.); suxinyu@stumail.ysu.edu.cn (X.S.)
* Correspondence: sxf@ysu.edu.cn

Abstract: In order to meet the demands of the bidirectional transmission of electric vehicle charger power, a series-resonant dual-active-bridge (DAB) converter is investigated in this paper. Firstly, the active and reactive power and zero voltage switching (ZVS) conditions of the full-bridge arm under extended phase-shift modulation, dual phase-shift modulation and triple phase-shift modulation are analyzed. Secondly, with the minimum reactive power as the optimization objective, the extended phase shift (EPS) is finally selected as the modulation method after comparing the minimum reactive power under various modulation methods when the normalized value of active power is varied in the range of 0–1. By constructing the objective function and determining the constraints, an off-line reactive power–minimization control strategy is proposed to achieve the ZVS of the full-bridge arm and, finally, the feasibility of the proposed control strategy is verified by simulation and experiment.

Keywords: dual-active-bridge converter; series resonance; phase shift modulation; zero voltage switching (ZVS); minimum reactive power

1. Introduction

A dual-active-bridge (DAB) DC–DC converter [1] is widely used in electric vehicles, energy storage systems, microgrid and other fields because it can realize bidirectional power transmission. It has the advantages of high modularity, easy ZVS soft switching, electrical isolation of input and output and so on. In the wide gain range and wide load range, the traditional single phase shift (SPS) has only one inter bridge phase-shift angle, which reduces the soft-switching range of the switching tube of the DAB converter, and the problem of the return power of the DAB converter under this control is more serious [2]. Therefore, scholars generally expand the soft-switching range of the DAB converter through modulation strategies [3–6], such as extended phase shift (EPS), dual phase shift (DPS) and triple phase shift (TPS), so as to improve power transmission efficiency. In order to further improve the efficiency of DAB converters, various optimized phase-shift control strategies have been proposed one after another. The essence of these optimization algorithms is to make the DAB converter always work on the optimal control point, thus reducing losses and improving efficiency. For example, reference [7] proposed a PWM phase-shift control, which adds the duty cycle control of the output to the phase-shift control, where both the phase-shift angle and duty cycle are used to reduce the current stress. Among the various optimal control strategies, the current RMS-optimized control is the most common [8,9]. However, the derivation process of current RMS-optimized control is complex and requires a high precision current detection circuit. Therefore, in recent years, reactive power optimal control has attracted more and more attention. Reference [10] analyzed and optimized the return power of a DAB converter under EPS modulation, which can effectively improve the transmission efficiency. Reference [11] proposed an optimal control scheme based on TPS modulation. References [12,13] propose reactive power–optimized control, but these papers define the return power as reactive power. However, reactive power defined in

this way exists only when the polarity of voltage and current are reversed. In reality, the presence of the inductor causes the converter to always absorb reactive power, regardless of the power transfer level, and reactive power values are always present and fluctuating. In reference [14], an optimal control strategy for a TPS-modulated DAB converter with reactive power expression as the objective function is proposed, which significantly improves the efficiency of the converter at light load and wide gain. Reference [15] searches for the minimum value of the rms value of the inductor current and finally derives the expressions between each phase-shift angle when the current rms value is minimum, but does not decouple the expressions from each other, so the relationship between the phase-shift angle and the transmitted power cannot be obtained quantitatively, and the control is not convenient.

In recent years, in order to improve the efficiency of DAB converters and improve the circuit power density, resonant the DAB converter has gradually become a research hotspot. Among them, the resonant dual-active-bridge converter composed of a DAB and an LC resonant tank only adds one resonant capacitance to the DAB topology. The DAB converter can be regarded as a limit case when the capacitance is infinite, so the series-resonant DAB converter has all the advantages of the DAB. Reference [16] points out that increasing the resonant capacitance can make the resonant current close to the sine wave and effectively filter out the DC current component of the transformer; moreover, it can reduce the eddy-current loss of transformer winding and help to reduce the off loss of the switch. However, the resonant DAB has the same problems as the traditional DAB. For example, the soft-switching range are reduced under light load, and when the voltages of the primary and secondary sides of the transformer do not match, the reactive power is large, which has a great impact on the efficiency of the converter.

This paper selects a series-resonant DAB converter as the research object and analyzes the relationship between the phase-shift modulation method and the minimum reactive power and soft switching of the full-bridge arm when the output power changes from no-load to full-load by comparing the active power and reactive power under three modulation methods of EPS, DPS and TPS so as to select an optimal modulation method for reactive power optimization, and give the specific optimization. The final combination of phase-shift angle for minimum reactive power is obtained to reduce the proportion of reactive power in the converter operation and thus improve the system efficiency.

2. Basic Characteristics of the Converter and Reactive Power Analysis

2.1. Introduction of Series-Resonant Dual-Active-Bridge Converter Topology

Figure 1 shows the circuit schematic diagram of the series-resonant DAB converter in which the input voltage V_{in}, the output voltage V_o, the resonant inductance Lr, the resonant capacitor C_r and the transformer on the original side turns a ratio of $n = N_1/N_2$. Enter the power and output power supply side in parallel one filter capacitor C_{in} and C_o. Defining the voltage gain of the converter is $M = nV_o/V_{in}$. The four bridge arms of the dual active bridge are represented by A, B, C and D, respectively.
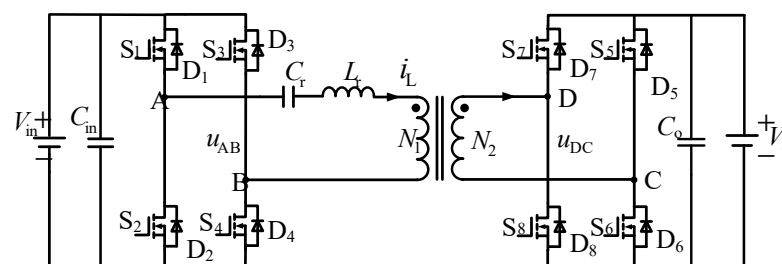

Figure 1. Series-resonant-type dual-active-bridge converter topology.

In this paper, phase-shift modulation is adopted, the duty ratio of all switching tubes is 50% and the upper and lower tubes of the same bridge arm are complementary conductive.

In phase-shift modulation, three control variables are involved: phase-shift angle φ_{AD} between bridges, phase-shift angles φ_{AB} within bridges and φ_{DC}. Define φ_{AD} as the phase-shift angle between S1 of bridge arm A and S7 of bridge arm D, and the range is $-\pi < \varphi_{AD} < \pi$; φ_{AB} is defined as the phase-shift angle between upper tube S1 of bridge arm A and upper tube S3 of bridge arm B, the range is $0 < \varphi_{AB} < 2\pi$; φ_{DC} is defined as the phase-shift angle between upper tube S7 of bridge arm D and upper tube S5 of bridge arm C, and the range is $0 < \varphi_{DC} < 2\pi$.

Because the harmonic content of resonant converter is low, this paper adopts fundamental wave analysis method to analyze and converts the secondary side of the transformer to the original side. The equivalent circuit is shown in Figure 2, where, $u_1(t)$ is the fundamental component of u_{AB}, $u_2(t)$ is the fundamental component of $n*u_{CD}$ and i_L is the fundamental component of resonant current. The resonant groove impedance is $X = \omega L_r - \frac{1}{\omega C_r}$.
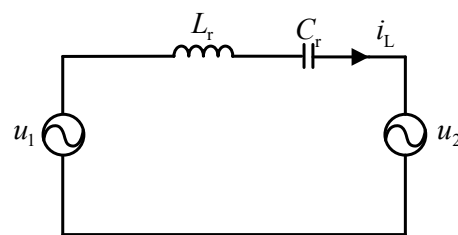

Figure 2. Series-connected resonant dual-active-bridge converter equivalent circuit diagram.

2.2. Steady-State Mathematical Model under Three Modulation Strategies

The working waveform of the series-resonant DAB converter in EPS modulation is shown in Figure 3, where u_A, u_B, u_C and u_D are the drive signals of the four bridge arms, u_{AB} and u_{CD} are the midpoint voltages of the arms of two active bridges and i_L is current flowing through the inductance.
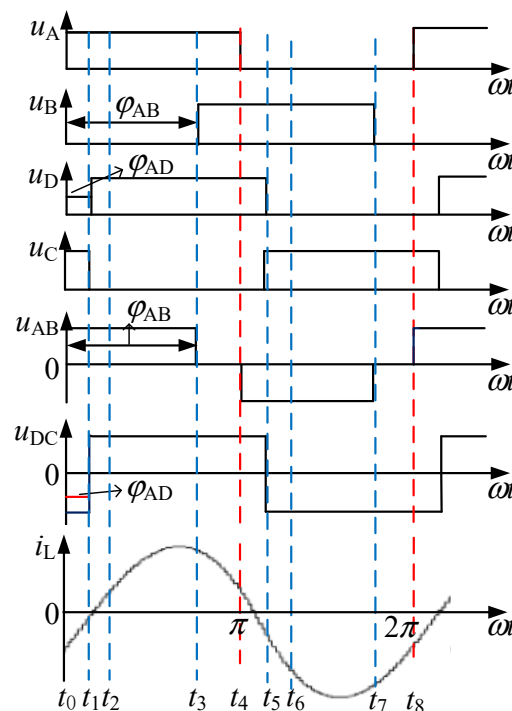

Figure 3. Work waveform under EPS modulation.

The converter has 8 operating modes per cycle under EPS phase-shift control, of which the operating modes from t_0 to t_4 are completely symmetrical with t_5 to t_8, and only the first four are analyzed.

(1) t_0–t_1 phase

The t_0 moment is the initial moment, before this state, S_2 and D_4 are on, while the resonant current is negative, at the t_0 moment, S_2 is disconnected and the driving signal reaches S_1; but since the current cannot be changed suddenly, the resonant slot current is still negative, so D_1 and D_4 are on. The secondary side of the transformer D_5 and D_8 are on, the voltage direction applied to both ends of the resonant slot is opposite to the current flow, resulting in the absolute value of current gradually decreasing, and when it decreases to 0, the energy is fed back from the resonant tank to the current side, and D_1, D_4, D_5 and D_8 are on in this stage.

(2) t_1–t_2 stage

At the moment of t_1, the trigger pulse reaches S_7, the current is naturally transferred to S_7, S_6 conduction, the primary state of the transformer remains unchanged, and the circulation path of the secondary side becomes S_7, S_6 This state continues until the voltage of the secondary side is reduced to the transformer induction voltage and this stage ends. In this stage, D_1, D_4, S_7 and S_6 are in the conduction state.

(3) t_2–t_3 phase

At the moment of t_2, the absolute value of resonant current decreases to 0. S_1 and S_4 realize zero voltage switching; the resonant current is about to increase positively, and the transformer secondary current flow path becomes D_7 and D_6. S_1, S_4, D_7 and D_6 are on in this stage.

(4) t_3–t_4 phase

At moment t_4, S_4 is disconnected. At this time the inductor current is positive, causing the current path to switch from S_4 to D_3, with S_1 and D_3 on for the high-voltage side, and D_5 and D_8 on for the low-voltage side. At the same time, the resonant tank current starts to decrease gradually from the peak due to the voltage applied to both ends of the resonant tank and the opposite direction of the resonant current flow. In this stage S_1, D_7, D_3 and D_6 are on.

According to the steady-state working waveform combined with fundamental wave analysis, the time-domain expressions of the two fundamental wave voltages in Figure 2 are shown in Equations (1) and (2):

$$u_{1.\text{EPS}}(\omega t) = \frac{4V_{\text{in}}}{\pi} \sin\left(\frac{\varphi_{\text{AB}}}{2}\right) \sin\left(\omega t + \frac{\pi - \varphi_{\text{AB}}}{2}\right) \tag{1}$$

$$u_{2.\text{EPS}}(\omega t) = \frac{4MV_{\text{in}}}{\pi} \sin(\omega t - \varphi_{\text{AD}}) \tag{2}$$

In order to calculate the complex power using the phase volume method, the phase volumes of the fundamental voltages $u_1(\omega t)$ and $u_2(\omega t)$ are defined here as $\dot{U}_1$ and $\dot{U}_2$, and the expressions for both are shown in Equations (3) and (4):

$$\dot{U}_{1.\text{EPS}} = \frac{\sqrt{2}}{\pi}[(1 - \cos\varphi_{\text{AB}}) + j\sin\varphi_{\text{AB}}] \tag{3}$$

$$\dot{U}_{2.\text{EPS}} = \frac{2\sqrt{2}MV_{\text{in}}}{\pi}[\cos(\varphi_{\text{AD}}) - j\sin(\varphi_{\text{AD}})] \tag{4}$$

The phasor of the fundamental wave component i_L of resonant current is defined as $\dot{I}_L$, and its expression is shown in Equation (5):

$$\dot{I}_L = \frac{\dot{U}_1 - \dot{U}_2}{jX} \tag{5}$$

According to Figure 2, the complex power transmitted by the AB bridge from the input side can be expressed as Equation (6):

$$\dot{S} = \dot{U}_1 \times \dot{I}_L^* \tag{6}$$

By solving this, the active power and reactive power expressions of which can be obtained as Equations (7) and (8), respectively.

$$P_{\text{EPS}} = \frac{4MV_{\text{in}}^2[\sin \varphi_{\text{AD}} + \sin(\varphi_{\text{AB}} - \varphi_{\text{AD}})]}{\pi^2 X} \tag{7}$$

$$Q_{\text{EPS,pu}} = \frac{4MV_{\text{in}}^2}{\pi^2 X}[\cos(\varphi_{\text{AB}} - \varphi_{\text{AD}}) - \cos(\varphi_{\text{AD}})] + \frac{4V_{\text{in}}^2}{\pi^2 X}[1 - \cos(\varphi_{\text{AB}})] \tag{8}$$

Taking $P_{\text{base}} = 8MV_{\text{in}}^2/\pi^2 X$ as the power reference value, the expressions of the normalized value of active power $P_{\text{EPS,pu}}$ and reactive power $Q_{\text{EPS,pu}}$ under EPS modulation are shown in Equations (9) and (10):

$$P_{\text{EPS,pu}} = 0.5 \sin \varphi_{\text{AD}} + 0.5 \sin(\varphi_{\text{AB}} - \varphi_{\text{AD}}) \tag{9}$$

$$Q_{\text{EPS,pu}} = 0.5 \cos(\varphi_{\text{AB}} - \varphi_{\text{AD}}) - 0.5 \cos(\varphi_{\text{AD}}) + \frac{1}{2M}[1 - \cos(\varphi_{\text{AB}})] \tag{10}$$

The working waveform of series-resonant DAB converter under DPS modulation is shown in Figure 4.
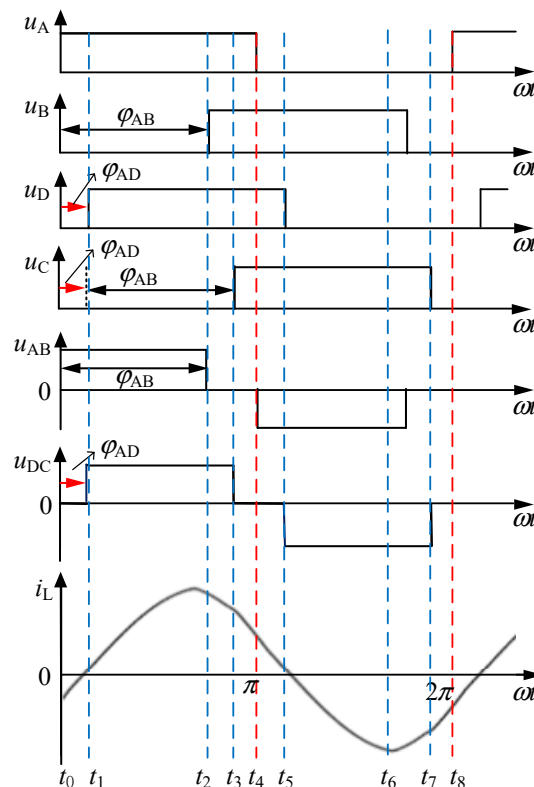

Figure 4. Work waveform under DPS modulation.

The converter operating modes are analyzed according to the steady-state operating waveform, which is divided into eight operating modes for each cycle under DPS modulation, of which the operating modes from t_0 to t_4 are completely symmetrical with t_5 to t_8.

(1)　Phase 1: t_0–t_1

At the moment of t_0, the converter transitions from mode 8 to mode 1, S_1 and S_4 are on, the inductor current is negative at this time, diodes D_5 and D_8 are on, and switching tube S_1 achieves zero voltage turn-on. The transformer secondary side switching tubes S_6 and S_7 are in continuous conduction. Power flows from the inductor to the secondary side.

(2)　Phase 2: t_1–t_2

Transformer primary side full-bridge switching tubes S_1 and S_4 continue to conduct, transformer secondary side switching tubes S_6 and S_7 conduct. t_1 moment inductor current comes to over zero, and both sides of the transformer at the same time charge the inductor current.

(3)　Stage 3: t_2–t_3

Transformer primary side full-bridge switching tube S_2 is on, transformer secondary side switching tubes S_6 and S_7 are continuously on. The inductor current charges the primary side and the power flows from the inductor to the primary side.

(4)　Stage 4: t_3–t_4

Transformer primary side full-bridge switching tube S_2 is on, transformer secondary side switching tube S_5 is on. The inductor current charges the secondary side.

Similarly, the time-domain expressions of the two fundamental voltages under DPS modulation can be derived as shown in Equations (11) and (12):

$$u_{1,\text{DPS}}(\omega t) = \frac{4V_{\text{in}}}{\pi} \sin\left(\frac{\varphi_{\text{AB}}}{2}\right) \sin\left(\omega t + \frac{\pi - \varphi_{\text{AB}}}{2}\right) \tag{11}$$

$$u_{2,\text{DPS}}(\omega t) = \frac{4MV_{\text{in}}}{\pi} \sin\left(\frac{\varphi_{\text{AB}}}{2}\right) \times \sin\left(\omega t - \varphi_{\text{AD}} + \frac{\pi - \varphi_{\text{AB}}}{2}\right) \tag{12}$$

The same power reference values as for EPS modulation are chosen. The derived expressions for the normalized value of active power $P_{\text{DPS,pu}}$ and reactive power $Q_{\text{DPS,pu}}$ under DPS modulation are given in (13) and (14) below:

$$P_{\text{DPS,pu}} = 0.5 \times (1 - \cos \varphi_{\text{AB}}) \times \sin \varphi_{\text{AD}} \tag{13}$$

$$Q_{\text{DPS,pu}} = \frac{1}{2M}(1 - \cos \varphi_{\text{AB}}) - 0.5 \times (1 - \cos \varphi_{\text{AB}}) \times \cos \varphi_{\text{AD}} \tag{14}$$

The working waveform of the series-resonant DAB converter under TPS modulation is shown in Figure 5.

The model is mainly divided into 10 working states, of which the first 1–5 working states and 6–10 working states are symmetrical, so only the first 5 working states are analyzed.

(1)　Phase 1: t_0–t_1

At the moment of t_0, the converter transitions from mode 10 to mode 1, S_2 turns off, the inductor current is negative at this time, diode D_1 conducts, and switching tube S_1 achieves zero voltage turn-on. Switching tubes S_6 and S_7 on the secondary side of the transformer are continuously on. Power flows from the inductor to the secondary side.

(2)　Phase 2: t_1–t_2

At moment t_1, the primary side of the full-bridge switching tube S_3 off, at this time the inductor current is negative, diode D_4 is in natural conduction, switching tube S_4 achieves

zero-voltage opening, the transformer secondary side switching tubes S_6 and S_7 continue to conduct.

(3)   Phase 3: t_2–t_3

Transformer primary side full-bridge switching tube S_1, S_4 continue to conduct, transformer secondary side switching tubes S_6 and S_7 continue to conduct. t_2 moment inductor current comes to over the zero point and both sides of the transformer at the same time charge the inductor current.

(4)   Phase 4: t_3–t_4

At moment t_3, the secondary side switching tube S_6 off, S_5 voltage discharge at both ends to 0, diode D_5 natural conduction, switching tube S_5 to achieve zero voltage open, the transformer primary side switching tube S_1, S_4 continue to conduct, to charge the inductor.

(5)   Phase V: t_4–t_5

At moment t_4, the secondary side of the full-bridge switching tube S_7 off, the voltage at both ends of S_8 discharge to 0, diode D_8 natural conduction, switching tube S_8 to achieve zero voltage open, the transformer primary side S_1, S_4 continue to conduct.
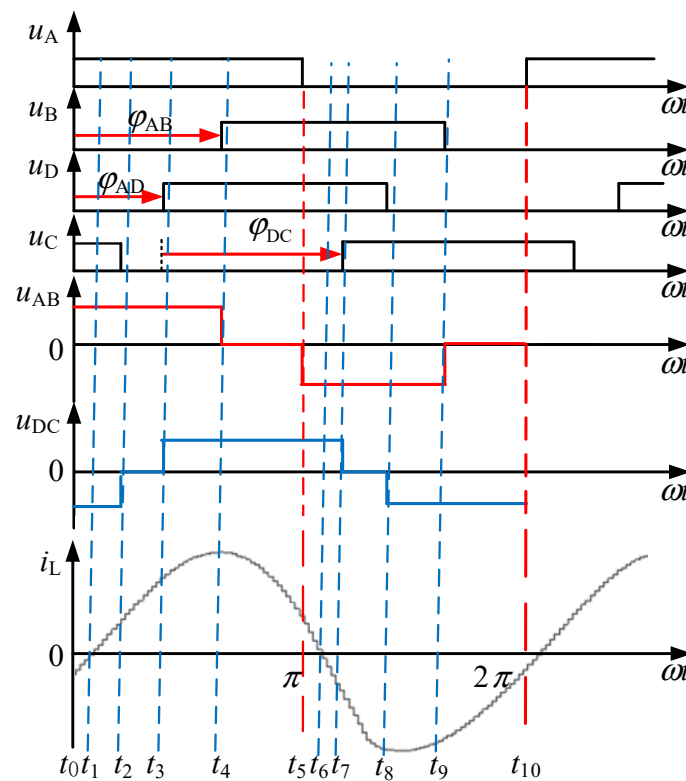

Figure 5. Work waveform under TPS modulation.

Similarly, the time domain expressions of the two fundamental wave voltages under TPS modulation can be derived (15) and (16) shown:

$$u_{1,\text{TPS}}(\omega t) = \frac{4V_{\text{in}}}{\pi} \sin\left(\frac{\varphi_{\text{AB}}}{2}\right) \sin\left(\omega t + \frac{\pi - \varphi_{\text{AB}}}{2}\right) \tag{15}$$

$$u_{2,\text{TPS}}(\omega t) = \frac{4MV_{\text{in}}}{\pi} \sin\left(\frac{\varphi_{\text{DC}}}{2}\right) \times \sin\left(\omega t - \varphi_{\text{AD}} + \frac{\pi - \varphi_{\text{DC}}}{2}\right) \tag{16}$$

The same power reference values as for EPS modulation are chosen. The expressions for the normalized value of active power $P_{\text{TPS,pu}}$ and reactive power $Q_{\text{TPS,pu}}$ under TPS modulation are derived as follows (17) and (18).

$$P_{\text{TPS,pu}} = 0.25 \times [\sin(\varphi_{AD} + \varphi_{CD} - \varphi_{AB}) + \sin\varphi_{AD} + \sin(\varphi_{AB} - \varphi_{AD}) - \sin(\varphi_{AD} + \varphi_{CD})] \quad (17)$$

$$\begin{aligned}Q_{\text{TPS,pu}} &= 0.25[-\cos(\varphi_{AD} + \varphi_{CD} - \varphi_{AB}) - \cos\varphi_{AD} + \cos(\varphi_{AB} - \varphi_{AD}) \\ &+ \cos(\varphi_{AD} + \varphi_{DC}) + \tfrac{1}{2M}(1 - \cos\varphi_{AB})]\end{aligned} \quad (18)$$

2.3. Analysis of Soft-Switching Characteristics under Three Modulation Strategies

In order to realize zero voltage switching (ZVS) of all switches, the anti-parallel diode of each switch needs to be turned on before the switch itself. Therefore, according to the positive current direction shown in Figure 1, it can be seen that in order to realize ZVS, a bridge arm needs to ensure that the inductive current $i_L < 0$ at the moment when the upper tube S_1 is turned on; to realize ZVS for bridge arm B, it is necessary to ensure that the inductor current $i_L > 0$ at the moment when the upper tube S_3 is turned on. To realize ZVS for D bridge arm, it is necessary to ensure that the inductance current $i_L > 0$ at the moment when the upper tube S_7 is turned on; to realize ZVS for bridge arm C, it is necessary to ensure that the inductor current $i_L < 0$ at the moment when the upper tube S_5 is turned on.

According to Figure 3, the conditions for realizing full-bridge arm ZVS under EPS modulation mode can be obtained, as shown in Equation (19). The full-bridge arm ZVS area drawn by Matlab is shown in Figure 6. The curves of various colors in the figure are the boundary lines of each bridge arm to realize ZVS.

$$\begin{cases} -\sin^2\left(\frac{\varphi_{AB}}{2}\right) + M\cos(\varphi_{AD}) < 0 & \text{A bridge leg} \\ \sin^2\left(\frac{\varphi_{AB}}{2}\right) + M\cos(\varphi_{AB} - \varphi_{AD}) > 0 & \text{B bridge leg} \\ \sin\left(\frac{\varphi_{AB}}{2}\right) \times \sin\left(\varphi_{AD} - \frac{\varphi_{AB}}{2}\right) + M > 0 & \text{C, D bridge leg} \end{cases} \quad (19)$$
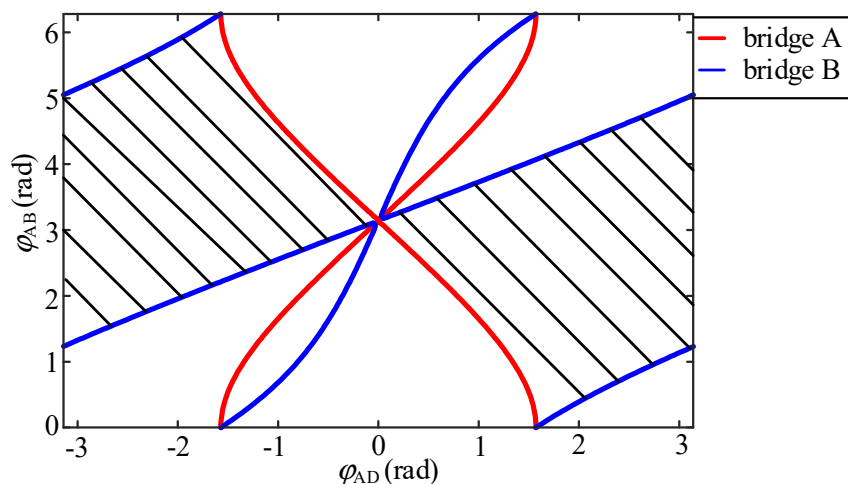

Figure 6. ZVS area under EPS modulation.

According to Figure 4, the conditions for realizing ZVS of full-bridge arm in DPS modulation mode can be obtained, as shown in Equation (20):

$$\begin{cases} -\sin^2\left(\frac{\varphi_{AB}}{2}\right) + M\sin\left(\frac{\varphi_{AB}}{2}\right)\sin(\phi_{AB}/2 + \phi_{AD}) < 0 & \text{A bridge leg} \\ \sin^2\left(\frac{\varphi_{AB}}{2}\right) - M\sin\left(\frac{\varphi_{AB}}{2}\right)\sin\left(\frac{\varphi_{AB}}{2} - \varphi_{AD}\right) > 0 & \text{B bridge leg} \\ \sin\left(\frac{\varphi_{AB}}{2}\right)\sin\left(\varphi_{AD} - \frac{\varphi_{AB}}{2}\right) + M\sin^2\left(\frac{\varphi_{AB}}{2}\right) > 0 & \text{C bridge leg} \\ \sin\left(\frac{\varphi_{AB}}{2}\right)\sin\left(\varphi_{AD} + \frac{\varphi_{AB}}{2}\right) - M\sin^2\left(\frac{\varphi_{AB}}{2}\right) < 0 & \text{D bridge leg} \end{cases} \quad (20)$$

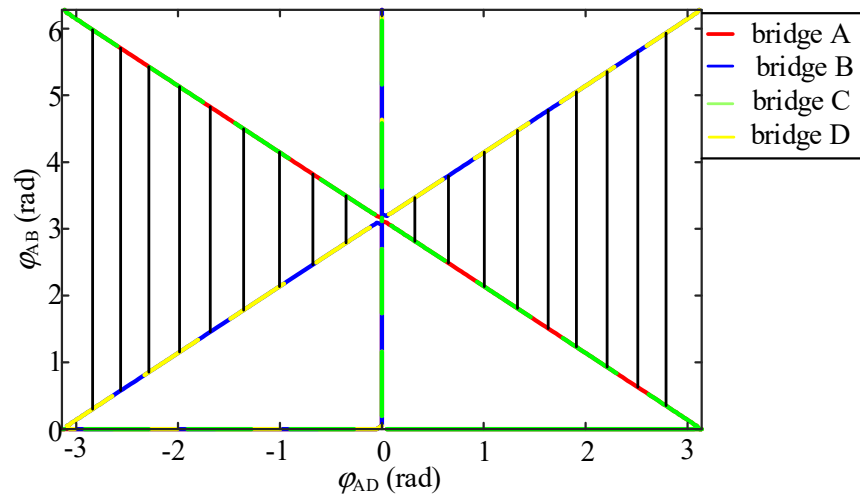The full-bridge arm ZVS area drawn by MATLAB is shown in Figure 7.

Figure 7. ZVS area under DPS modulation.

According to Figure 5, the conditions for realizing ZVS of the full-bridge arm in TPS modulation mode can be obtained, as shown in Equation (21):

$$
\begin{cases}
-\sin^2(\frac{\phi_{AB}}{2}) + \sin(\frac{\phi_{DC}}{2})\sin(\phi_{AD} + \frac{\phi_{DC}}{2}) < 0 & \text{A bridge leg} \\
\sin^2(\frac{\phi_{AB}}{2}) + \sin(\frac{\phi_{DC}}{2})\sin(\frac{\phi_{DC}}{2} + \phi_{AD} - \phi_{AB}) > 0 & \text{B bridge leg} \\
\sin(\frac{\phi_{AB}}{2})\sin(\phi_{AD} - \frac{\phi_{AB}}{2}) + \sin^2(\frac{\phi_{DC}}{2}) > 0 & \text{C bridge leg} \\
\sin(\frac{\phi_{AB}}{2})\sin(\phi_{AD} + \phi_{DC} - \frac{\phi_{AB}}{2}) - \sin^2(\frac{\phi_{DC}}{2}) < 0 & \text{D bridge leg}
\end{cases}
\tag{21}
$$

Since TPS contains three control quantities, in order to display the soft-switching area in the two-dimensional coordinate system, it is taken here that $\varphi_{DC} = 90°$ for simulation. The ZVS area of the full-bridge arm drawn by Matlab is shown in Figure 8.
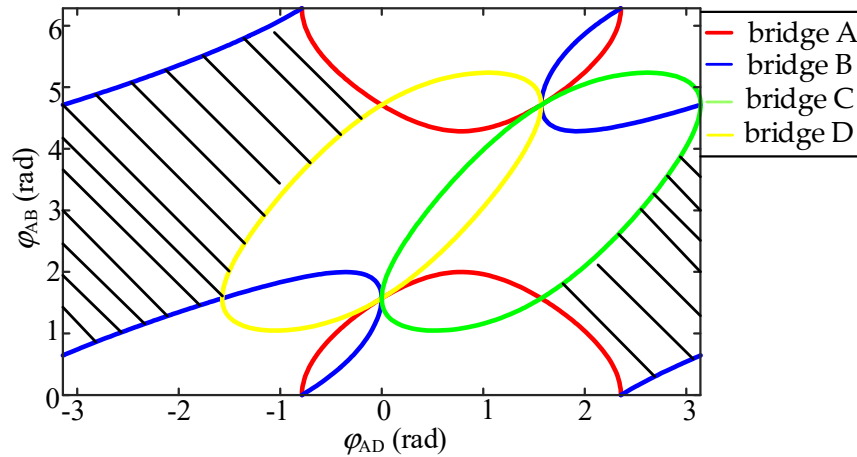
Figure 8. Closeroen arm ZVS area under TPS modulation.

By comparing Figures 6 and 7, it is not difficult to find that EPS modulation and DPS modulation have similar sizes in the soft-switching region of the full-bridge arm, while TPS modulation ($\varphi_{DC} = 90°$) has a smaller soft-switching region.

2.4. Minimum Reactive Power Analysis under Different Modulation Strategies

In order to analyze the minimum reactive power corresponding to the full-bridge ZVS under different modulation strategies, the unit value of active power is taken every 0.1 in the range of 0–1. Draw the full-bridge ZVS boundary line, the active power unit value curve and the reactive power contour line under the three modulation strategies in the same plane and, finally, obtain Figures 9–11. The normalized value of the active power

curve in the figure corresponds to a closed ellipse or oblique ellipse. Compare the minimum reactive power value of different modulation strategies when the gain $M = 1$. Through the reading of the data in Figures 9 and 10, the minimum reactive value intersected by the unit value of different active power can be obtained. Under TPS modulation, the internal phase-shift angle of the secondary side bridge is given as $\varphi_{DC} = 90°$, the area where all active power curves are located is the hard-switching area.
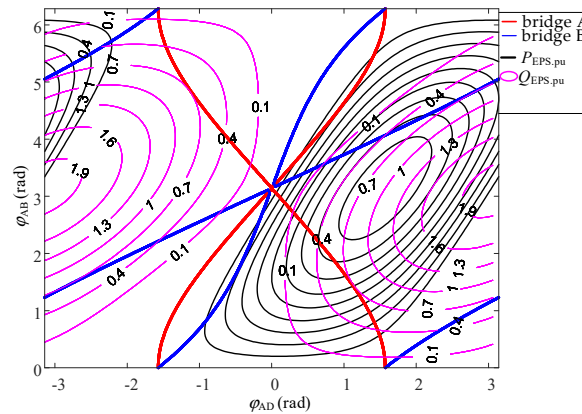

Figure 9. Intersection of active power and reactive power contours under EPS modulation ($M = 1$).
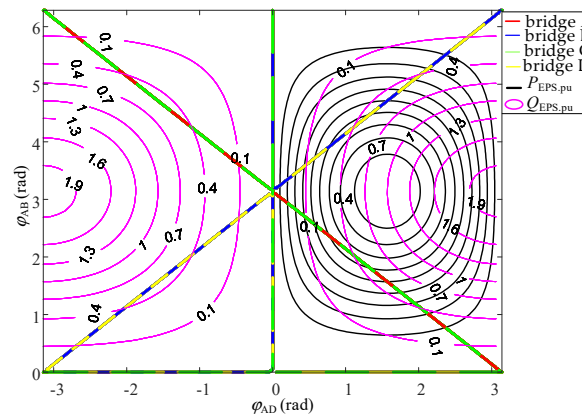
Figure 10. Intersection of active power and reactive power contours under DPS modulation ($M = 1$).
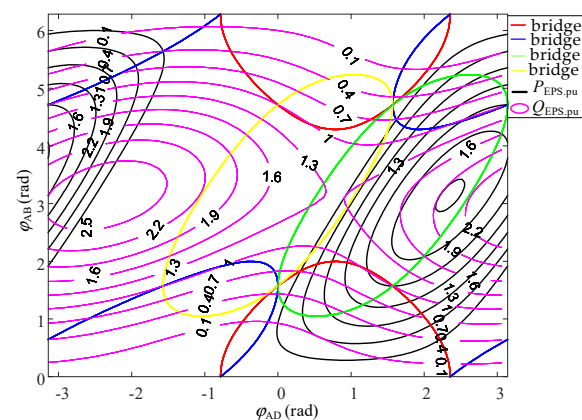
Figure 11. Intersection of active power and reactive power contours under TPS modulation ($M = 1$).

According to the soft-switching boundary lines, the normalized value of the active power curves and the reactive power contours of the above three modulation modes, the EPS modulation mode achieves the largest area of full-bridge ZVS and the smallest reactive power value among the three modulation modes. TPS modulation reduces the range of

the active power that can be transmitted due to the introduction of too many phase-shift angles and when $P_{\text{EPS.pu}} = 0.7$, all are located in the hard-switching area. The minimum reactive power values at different active power unit values for different modulation modes are shown in Table 1.

Table 1. The normalized value of active power and the minimum reactive power intersection value.

The Normalized Values of Active Power		0.1	0.2	0.3	0.4	0.5	0.6	0.7	0.8	0.9
Minimum reactive power value	EPS	0	0.018	0.05	0.07	0.12	0.20	0.27	0.39	0.52
	DPS	0	0.02	0.05	0.08	0.13	0.21	0.29	0.4	0.55
	TPS	0.4	0.62	0.77	0.9	1	1.6			

3. Optimal Reactive Power Control Strategy

3.1. Series-Resonant DAB Reactive Power Optimization Control Strategy

Determine the objective function studied in this paper as in Equation (22):

$$\text{Min}[Q_{\text{EPS}}(\varphi_{\text{AD}}, \varphi_{\text{AB}})] \tag{22}$$

When the system transmits a certain value of active power, the active power trajectory is used as the limiting condition of the equation. As in Equation (23):

$$P_{\text{o.pu}} = P_{\text{EPS.pu}}(\varphi_{\text{AD}}, \varphi_{\text{AB}}) \tag{23}$$

When the system transmits a certain value of active power, the active power value is taken as a known quantity, and the active power trajectory is taken as the limit condition of the equation, the functional expressions of the intra-bridge phase-shift angle φ_{AB} and the inter-bridge phase-shift angle φ_{AD} can be obtained, as in Equation (24):

$$\varphi_{\text{AB}} = f(\varphi_{\text{AD}}, P_{\text{EPS.pu}}) \tag{24}$$

Using $8MV_{\text{in}}^2/\pi^2X$ as the power reference value, the expression obtained is as in Equation (25):

$$P_{\text{EPS.pu}} = 0.5[\sin\varphi_{\text{AD}} + \sin(\varphi_{\text{AB}} - \varphi_{\text{AD}})] \tag{25}$$

Two expressions for the phase-shift angle φ_{AB} within the bridge can be obtained as in Equations (26) and (27):

$$\varphi_{\text{AB1}} = \arcsin(2P_{\text{EPS.pu}} - \sin\varphi_{\text{AD}}) + \varphi_{\text{AD}} \tag{26}$$

$$\varphi_{\text{AB2}} = \pi + \varphi_{\text{AD}} - \arcsin(2P_{\text{EPS.pu}} - \sin\varphi_{\text{AD}}) \tag{27}$$

The two expressions of the intra-bridge phase-shift angle φ_{AB} are substituted into the expression of the reactive power standardized value, and the expression of the reactive power relative to the inter-bridge phase-shift angle φ_{AD} is obtained as in Equations (28) and (29):

$$\begin{aligned} Q_{\text{EPS.pu1}} &= 0.5\cos\left[\arcsin(2P_{\text{EPS.pu}} - \sin\varphi_{\text{AD}})\right] - 0.5\cos\varphi_{\text{AD}} \\ &+ \frac{1}{2M}\left\{1 - \cos\left[\arcsin(2P_{\text{EPS.pu}} - \sin\varphi_{\text{AD}}) + \varphi_{\text{AD}}\right]\right\} \end{aligned} \tag{28}$$

$$\begin{aligned} Q_{\text{EPS.pu2}} &= 0.5\cos\left[\pi - \arcsin(2P_{\text{EPS.pu}} - \sin\varphi_{\text{AD}})\right] - 0.5\cos\varphi_{\text{AD}} \\ &+ \frac{1}{2M}\left\{1 - \cos\left[\pi + \varphi_{\text{AD}} - \arcsin(2P_{\text{EPS.pu}} - \sin\varphi_{\text{AD}})\right]\right\} \end{aligned} \tag{29}$$

The three curves above in Figure 12 are the images of $Q_{\text{EPS.pu1}}$, and the three curves below are the images of $Q_{\text{EPS.pu2}}$. From the above relationship between the reactive power standardized value $Q_{\text{EPS.pu}}$ and the inter-bridge phase-shift angle φ_{AD} under different gain M, it can be seen that when the gain $M = 1$, the image of $Q_{\text{EPS.pu2}}$ is always located below

the image of $Q_{EPS.pu1}$, indicating that the same inter-bridge phase shift The reactive power value of $Q_{EPS.pu2}$ is always smaller than that of $Q_{EPS.pu1}$ when the phase angle shifts phase angle, and when the gain M is 0.5, the image of $Q_{EPS.pu2}$ is located above the image of $Q_{EPS.pu1}$ in the 0.33–1.03 radian range, so the reactive power value of $Q_{EPS.pu2}$ is larger than that of $Q_{EPS.pu1}$ in this range, and when $M = 0.75$, the reactive power value of $Q_{EPS.pu1}$ in the reactive power value of $Q_{EPS.pu2}$ is greater than that of $Q_{EPS.pu1}$ in this range; when $M = 0.75$, in the range of 0.35–0.73 radians, the image of $Q_{EPS.pu2}$ is located above the image of $Q_{EPS.pu1}$, and the reactive power value of $Q_{EPS.pu2}$ is greater than that of $Q_{EPS.pu1}$ in this range. The smaller the gain M, the larger the range of $Q_{EPS.pu2}$, but from the size of the range of the two, the $Q_{EPS.pu2}$ reactive power standardized value is always smaller than the larger range, and when the gain $M = 1$, the full range of the $Q_{EPS.pu2}$ value is constantly smaller than $Q_{EPS.pu1}$.
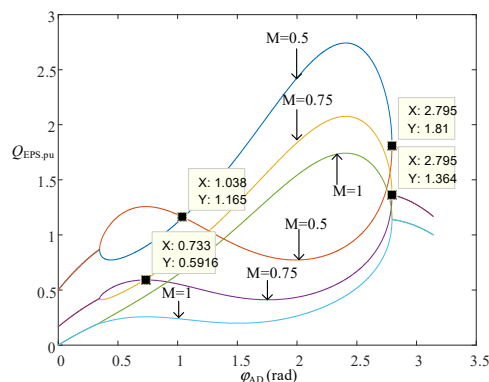
Figure 12. $P_{EPS.pu} = 0.67$ at different gain M, the relation curve between $Q_{EPS.pu}$ and the bridge phase-shift angle φ_{AD}.

Keep the gain $M = 1$ constant, change the active power standardized value, the reactive power standardized value $Q_{EPS.pu}$, and the relationship between the inter-bridge phase-shift angle φ_{AD} is shown in Figure 13.
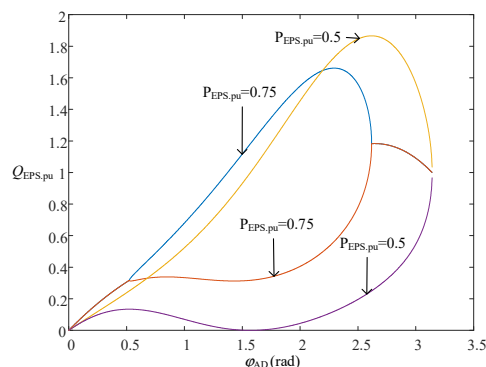

Figure 13. The relation curve between $Q_{EPS.pu}$ and the bridge phase-shift angle φ_{AD} under different monoid values of active power.

The top two curves in Figure 13 are images of $Q_{EPS.pu1}$ and the bottom two curves are images of $Q_{EPS.pu2}$. From Figure 13, it can be seen that changing the magnitude of the active power minimum value $Q_{EPS.pu}$ does not affect the trend of the curve of the gain reactive power minimum value $Q_{EPS.pu}$ and the inter-bridge phase-shift angle φ_{AD}, and the value of $Q_{EPS.pu1}$ is always larger than the value of $Q_{EPS.pu2}$ during the change of the inter-bridge phase-shift angle φ_{AD}. As the inter-bridge phase-shift angle φ_{AD} increases, the reactive power minimum value $Q_{EPS.pu}$ is always increasing.

In order to prove the reliability of the formula, this paper verifies the formula by building a simulation through matlab, given the input voltage $V_{in} = 100$ V, output voltage

$V_o = 100$ V and active power $P = 200$ W and finally verifies the reactive power data of equation $Q_{EPS.pu1}$ and equation $Q_{EPS.pu2}$ under different phase-shift angles when the gain $M = 1$, as shown in Table 2.

Table 2. Comparison of reactive power values at different phase-shift angles.

Inter-Bridge Phase-Shift Angle φ_{AD} (°)	Intra-Bridge Phase-Shift Angle φ_{AB1} (°)	Reactive Power $Q_{EPS.pu1}$ (Var)	Intra-Bridge Phase-Shift Angle φ_{AB2} (°)	Reactive Power $Q_{EPS.pu2}$ (Var)
30	76.9	100	163.1	65
60	81.9	200	219	57
90	103	340	257	43
120	141.34	495	278.66	67
150	196.88	539	283.12	146

From the simulation results in Table 2 for different inter-bridge phase-shift angles, it can be seen that the reactive power value of equation $Q_{EPS.pu1}$ is always greater than that of equation $Q_{EPS.pu2}$. The simulation waveforms are given here for the inter-bridge phase-shift angle $\varphi_{AD} = 30°$, intra-bridge phase-shift angle $\varphi_{AB1} = 76.9°$ and $\varphi_{AB2} = 163.1°$; inter-bridge phase-shift angle $\varphi_{AD} = 90°$, intra-bridge phase-shift angle $\varphi_{AB1} = 103°$ and $\varphi_{AB2} = 257°$; and the simulation waveforms are shown in Figures 14–17.
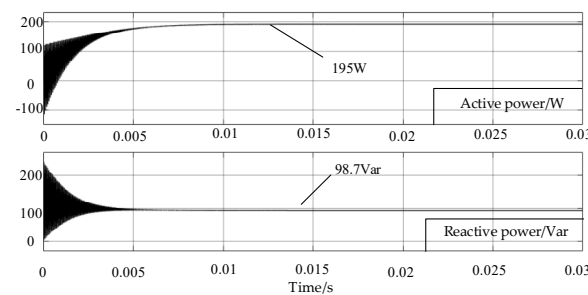
Figure 14. $\varphi_{AD} = 30°$, $\varphi_{AB} = 76.9°$ active power and reactive power waveforms.
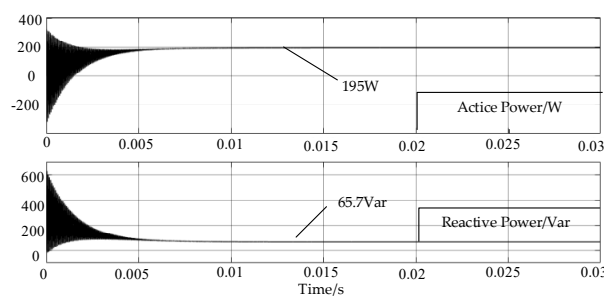
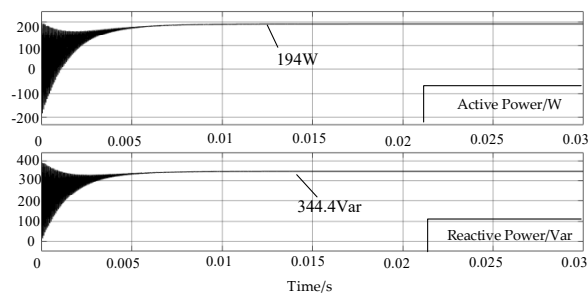**Figure 15.** $\varphi_{AD} = 30°$ and $\varphi_{AB} = 163.1°$ active power and reactive power waveforms.

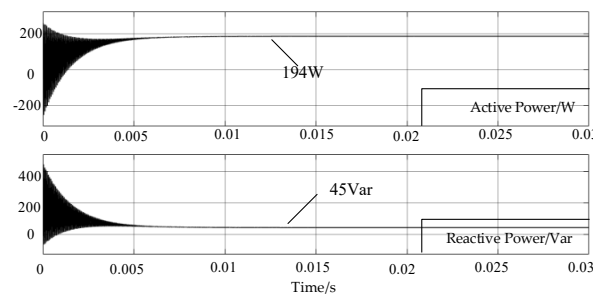**Figure 16.** $\varphi_{AD} = 90°$ and $\varphi_{AB} = 103°$ active power and reactive power waveforms.

Figure 17. $\varphi_{AD} = 90°$ and $\varphi_{AB} = 257°$ active power and reactive power waveforms.

Since there is a certain error between the theoretical calculation and the simulation value, the active power values in the above simulation results are slightly smaller than the theoretical values, but they are within the error range. According to the comparison between the above analysis and the simulation results, it can be seen that when the gain $M = 1$, among the two inter-bridge phase-shift angles corresponding to the same inter-bridge phase-shift angle φ_{AD}, the one with the larger inter-bridge phase-shift angle value has a smaller reactive power value. When the gain M is less than 1, the small region Qepspu1 is smaller than Qepspu2; therefore, this paper selects the reactive power needed to make a judgment about the gain M, and then compares the size of the reactive power values of Equations (28) and (29).

In the current power reference value, gain $M = 1$ for active power of 200 W and the corresponding active power standardized value is 0.62, so the intersection of the reactive power contour occurs when the normalized value of active power is 0.52, 0.62 and 0.72, respectively, is drawn as shown in Figure 18: the blue horizontal and vertical lines in the figure are the intra-bridge phase-shift angle $\varphi_{AB} = \pi$ and the inter-bridge phase-shift angle $\varphi_{AD} = \pi/2$.

The following conclusions can be drawn from Figure 18:

(1) In a certain active power standardized value, when the same inter-bridge phase-shift angle φ_{AD} corresponds to two intra-bridge phase-shift angles φ_{AB} and the larger the intra-bridge phase-shift angle, the smaller the value of the reactive power contour is handed over. Similarly, the same intra-bridge phase-shift angle φ_{AB} corresponds to two intra-bridge phase-shift angles φ_{AD} and the smaller value of the reactive power contour;

(2) At a certain active value in the intersection with the reactive power contour, the closer to the right side of the image, the greater the value of the reactive power; the closer to the left side of the image, the smaller the value of the reactive power;

(3) The minimum reactive power is located in the vicinity of the intra-bridge phase-shift angle $\varphi_{AB} = \pi$, which is near the single phase-shift modulation strategy.

According to the above analysis, a reactive power minimization control measurement is designed in this paper. When the output voltage and active power standard minimum values are given, the system automatically performs the optimization search and finally outputs a combination of phase-shift angles with the minimum reactive power under the condition of realizing the full-bridge arm ZVS so that the reactive power accounts for the minimum in the system and thus improves the efficiency of the system.

As can be seen from Figure 18, the obtained minimum reactive power value under the full-bridge arm of ZVS is located near the intra-bridge phase-shift angle $\varphi_{AB} = \pi$, and the difference between the minimum reactive power value under the full-bridge arm of ZVS is very small in its upper and lower seeking directions, so only the upper direction of seeking is performed in this paper, which is based on the obtained single phase-shift angle φ_{AD} plus delta phi. The experiments and simulations that follow compare the reactive power minima in the upper and lower directions to express the small differences between them. The flow chart of the reactive power minimization control strategy designed in this paper is shown in Figure 19 below.
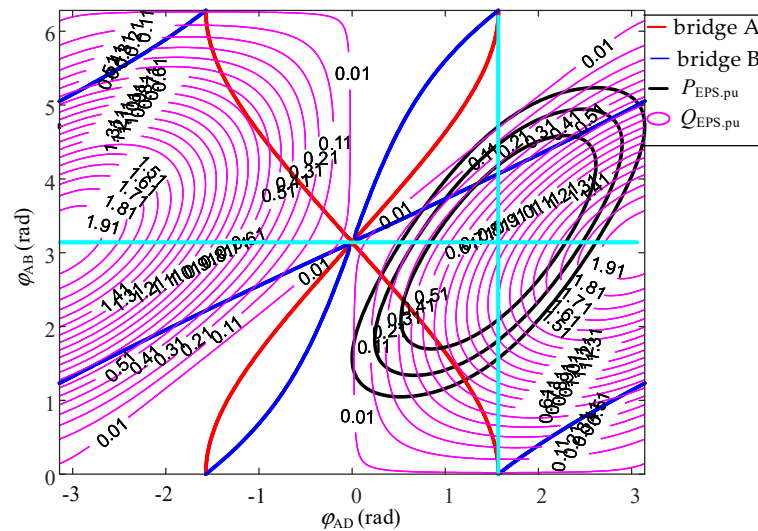
Figure 18. Intersection of different active power standardized values and reactive contour.

First, in the optimal reactive power control, input voltage, output voltage, transformer ratio and the normalized values of active power are first given to calculate the gain M. According to the active power expression of the single phase-shift control strategy, the inter-bridge phase-shift angle φ_{AD} can be found since the same active power output results in two inter-bridge phase-shift angles. According to the previous analysis, the smaller the inter-bridge phase-shift angle φ_{AD} is, the smaller the corresponding reactive power value is. Due to the optimization procedure, the system output inverse delta function results in the interval $[0–\pi/2]$. Make a determination of M. If M is not less than 1, substitute φ_{AD} into Formula (29), record the reactive power value as Q_{min} at this time, and then carry out the optimization solution cycle. Add a set step $\Delta\varphi$ to φ_{AD}, where the step $\Delta\varphi$ is given as 0.001 in the program, record it as φ_{AD} in the program, bring it into Formula (27) to get the corresponding intra-bridge phase-shift angle φ_{AB}, bring (φ_{AD}, φ_{AB}) into the full-bridge arm ZVS inequality to see if it satisfies the full-bridge arm ZVS inequality, and if it does, then bring (φ_{AD}, φ_{AB}) into Formula (29) and record the obtained $Q(\varphi_{AD})$ as Q' and compare it with Q_{min}, record the smaller one as Q_{min}, record the phase-shift angle at this time as φ_{AD}, then go back to φ_{AD} and add a set step $\Delta\varphi$, and so on until the obtained phase-shift angle does not meet the full-bridge arm ZVS output minimum reactive power value Q_{min} corresponding to the system, and give the number of times to seek and the corresponding best phase-shift angle combination according to the output requirements of the flow chart, and then look up in the table to get the best phase-shift angle combination corresponding to the minimum reactive power. If M is less than 1, put φ_{AD} into band Formulas (28) and (29), respectively, to get the corresponding $Q'(_{AD})$, and record the smaller value as Q'_{min}; then carry out another optimization solution cycle, add a set step to φ_{AD} similarly, $\Delta\varphi$, according to Formulas (26) and (27), to obtain the corresponding intra-bridge phase-shift angle φ_{AB}, Substitute (φ_{AD}, φ_{AB}) into the ZVS inequality of full-bridge arm, compare the minimum value of reactive power obtained by the two sets of phase-shift angles and remember the smaller value as Q'', compare it with Q'_{min} and remember the smaller value as Q'_{min}. This cycle is carried out until the obtained phase-shift angle does not meet ZVS and the minimum reactive power value Q'_{min} corresponding to the system is output. According to the output requirements of the flow chart, the times and the corresponding optimal phase-shift angle combinations are given, and then the optimal phase-shift angle combination corresponding to the minimum reactive power is obtained by searching in the table.
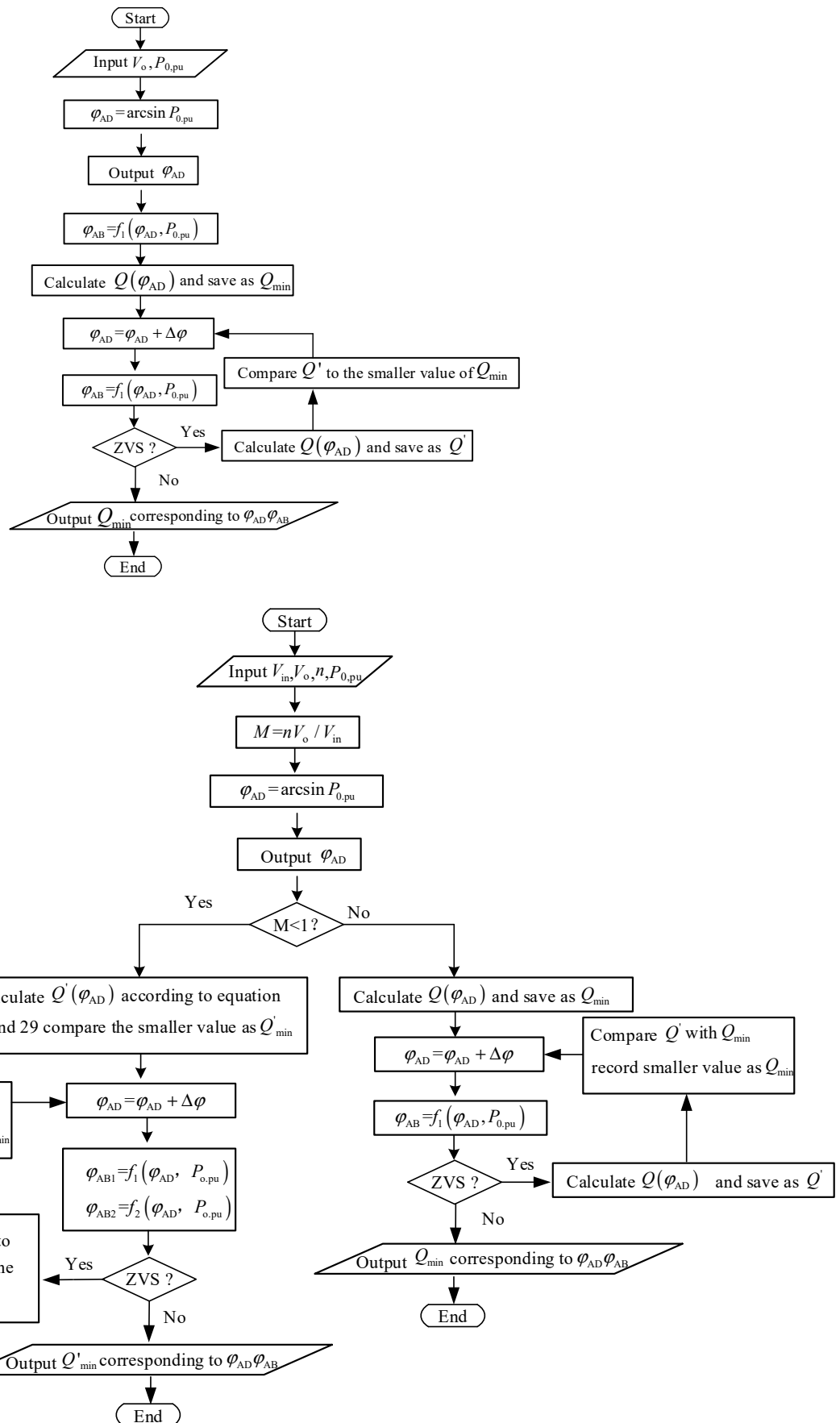
Figure 19. Reactive power minimization optimization seeking control flow.

3.2. Minimum Reactive Power Simulation Verification

According to the control strategy proposed in this paper, the simulation was built in MATLAB for the experiment, and the reactive power value was compared by comparing the obtained phase-shift angle combination with other randomly selected points of the phase-shift angle combination. When the gain $M = 1$, according to the obtained phase-shift angle combination brought into the simulation with the phase-shift angle combination of (25.8°, 152°), the obtained the active and reactive power simulations are as shown in Figure 20.
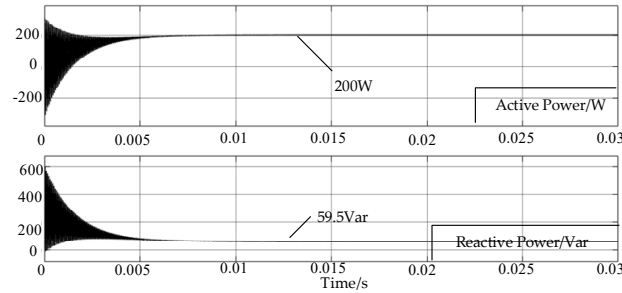
Figure 20. $\varphi_{AD} = 25.8°$ and $\varphi_{AB} = 152°$ active power and reactive power waveforms.

Observe the ZVS of each bridge arm, as shown in Figures 21–23 below.
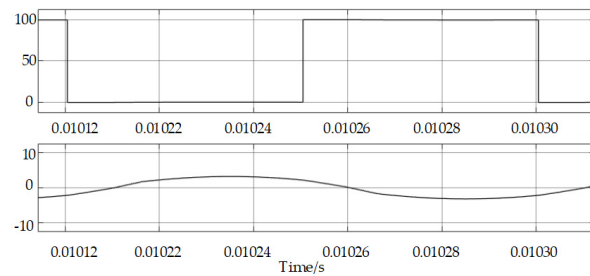
Figure 21. $\varphi_{AD} = 25.8°$ and $\varphi_{AB} = 152°$ bridge-arm A drain-source voltage and current waveforms.
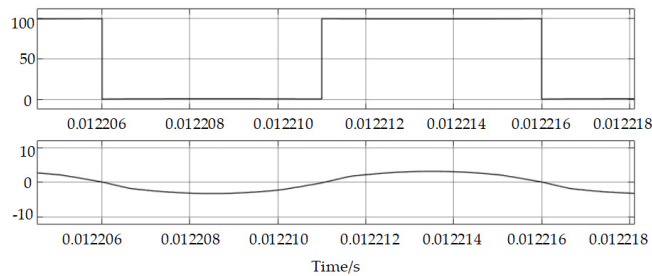
Figure 22. $\varphi_{AD} = 25.8°$ and $\varphi_{AB} = 152°$ bridge-arm B drain-source voltage and current waveforms.
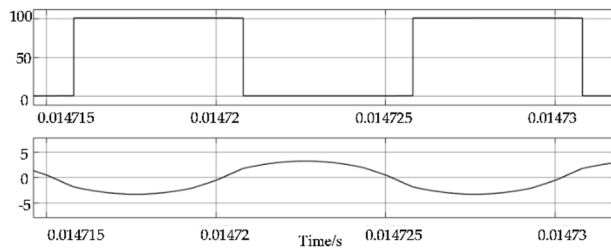
Figure 23. $\varphi_{AD} = 25.8°$ and $\varphi_{AB} = 152°$ bridge-arm C drain-source voltage and current waveforms.

When full-arm ZVS is achieved, the A-arm current changes from negative to positive after the A-arm drain-source voltage drops to 0. The B-arm current changes from positive

to negative after the B-arm drain-source voltage drops to 0. The C-arm current changes from negative to positive after the C-arm drain-source voltage drops to 0.

A combination of phase-shift angles within the ZVS range of the two full-bridge arms was randomly selected for the same power and gain, and the phase-shift angles ($\varphi_{AD} = 97.2°$, $\varphi_{AB} = 115°$) were chosen for the comparison of reactive power values, as shown in Figure 24.
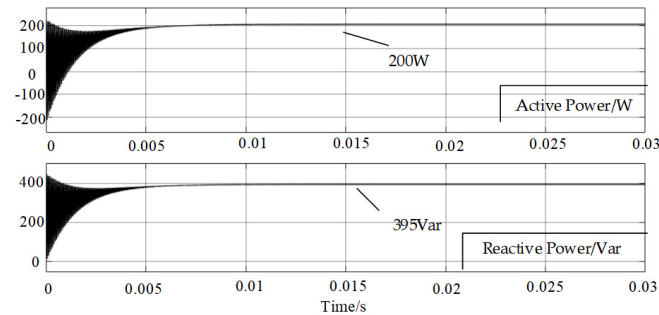

Figure 24. $\varphi_{AD} = 97.2°$ and $\varphi_{AB} = 115°$ active power and reactive power waveforms.

The selected phase-shift angles ($\varphi_{AD} = 31°$, $\varphi_{AB} = 80.2°$) for the comparison of reactive power values is shown in Figure 25.
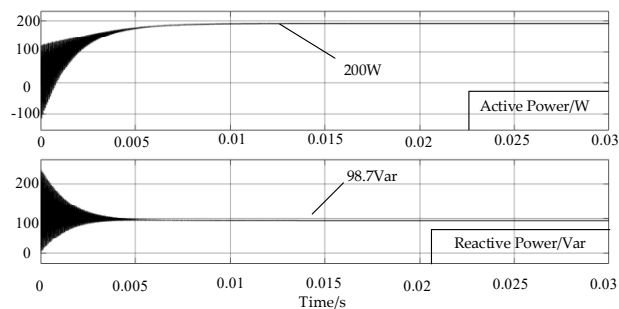
Figure 25. $\varphi_{AD} = 31°$ and $\varphi_{AB} = 80.2°$ active power and reactive power waveforms.

From the above simulation results, it can be seen that the reactive power value of the obtained phase-shift angle is significantly smaller than other combinations of phase-shift angles under the premise of achieving full-bridge arm ZVS. Although the obtained points may be located near the boundary of the A-bridge arm or B-bridge arm, the obtained results are located within the ZVS range, and the value of the reactive power is greatly reduced, which improves the overall efficiency of the system.

When the gain $M = 0.8$, the combination of phase-shift angles output from the flow chart is brought into the simulation, and the combination of phase-shift angles is ($92°$, $239°$), the simulation results of the active and reactive power obtained are as shown in Figure 26.
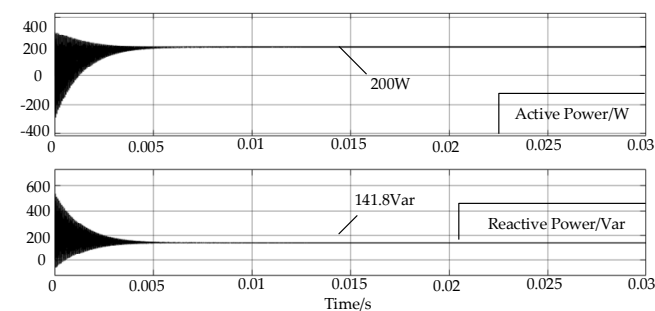

Figure 26. $\varphi_{AD} = 92°$ and $\varphi_{AB} = 239°$ active power and reactive power waveforms.

Observe the ZVS of each bridge arm as shown in Figures 27–29 below.

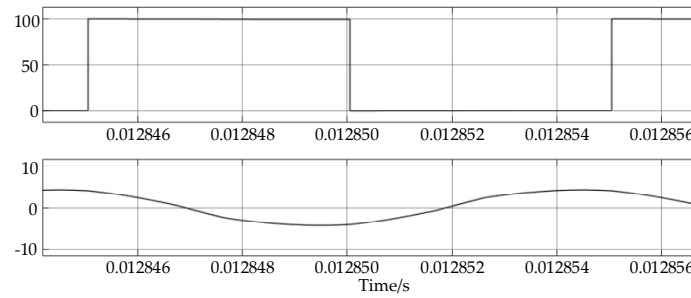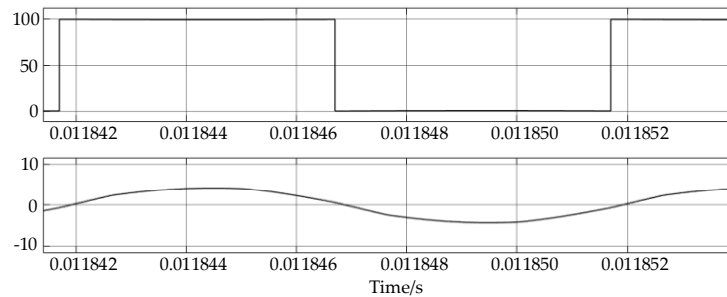**Figure 27.** $\varphi_{AD} = 92°$ and $\varphi_{AB} = 239°$ bridge-arm A drain-source voltage and current waveforms.

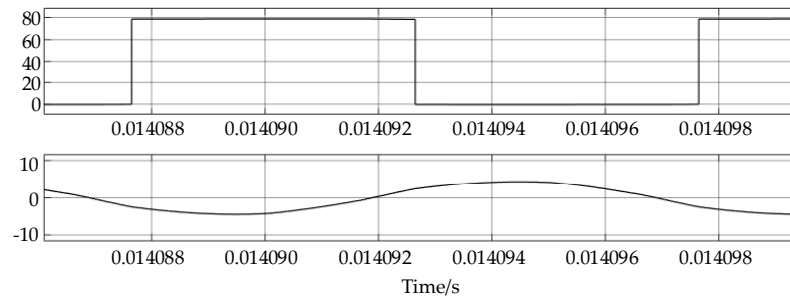**Figure 28.** $\varphi_{AD} = 92°$ and $\varphi_{AB} = 239°$ bridge-arm B drain-source voltage and current waveforms.

Figure 29. $\varphi_{AD} = 92°$ and $\varphi_{AB} = 239°$ bridge-arm C drain-source voltage and current waveforms.

When the full-arm ZVS is realized, the resonant current turns from negative to positive after the A-arm drain-source voltage drops to 0. After the B-arm drain-source voltage drops to 0, the resonant current is at the positive to negative boundary, and the B-bridge arm is at the soft-switching boundary at this time. After the C-bridge arm drain-source voltage drops to 0, the transformer secondary current turns from negative to positive.

In the ZVS range of the full-bridge arm, a combination of phase-shift angles with the same power and gain was randomly selected and the phase-shift angle ($\varphi_{AD} = 63°$, $\varphi_{AB} = 202.57°$) was chosen to compare the reactive power values, as shown in Figure 30.
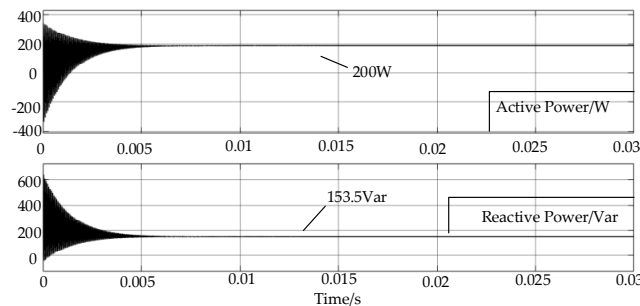

Figure 30. $\varphi_{AD} = 63°$ and $\varphi_{AB} = 202.57°$ active power and reactive power waveforms.

When the gain M = 0.8, it can be seen from the above simulation results that the reactive power value of the obtained phase-shift angle is significantly smaller than another set of phase-shift angle combinations under the premise of realizing the full-bridge arm ZVS, which improves the system efficiency.

When the gain M = 0.6, the simulations were performed for the combination of phase-shift angles (96.3°, 192°) and randomly selected phase-shift angles (92.4°, 195°) of the system output in the full-bridge arm ZVS range to compare the reactive power values, as shown in Figures 31 and 32.
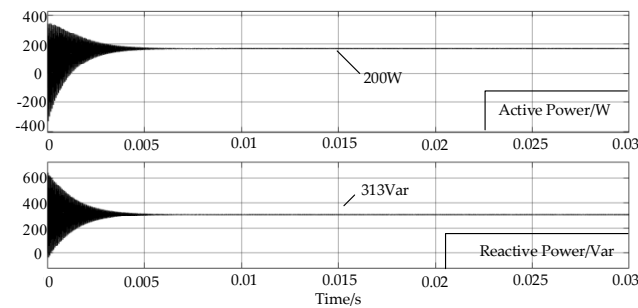

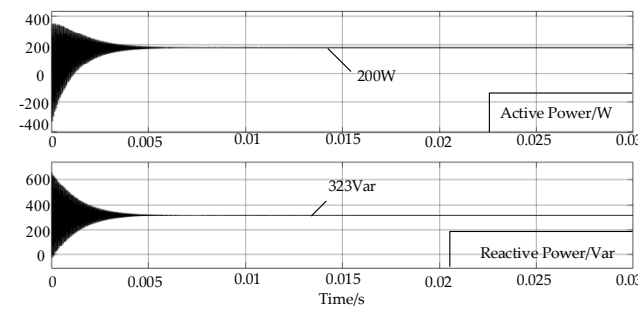**Figure 31.** φ_{AD} = 96.3° and φ_{AB} = 192° active power and reactive power waveforms.

Figure 32. φ_{AD} = 92.29° and φ_{AB} = 185° active power and reactive power waveforms.

When the gain M = 0.6, it can be seen from the simulation results in Figures 31 and 32 that the system output phase-shift angle combination has a smaller value of reactive power compared with the randomly selected phase-shift angle combination, so it can be proved that the system output phase-shift angle combination is more efficient.

From the above simulation, it can be seen that whether the gain M is less than 1 or the gain M is equal to 1, the reactive power output by the system with the combination of phase-shift angles is smaller than the combination of phase-shift angles randomly selected under the premise of satisfying the full-bridge arm ZVS, so the correctness of the control strategy can be proved.

According to the flowchart prepared in MATLAB, the simulation results for active power of 200 W for different output voltage ranges and for an output voltage of 100 V for different power cases were measured, as shown in Tables 3 and 4.

Table 3. Optimal combination of phase-shift angle at 200 W output power and 50–100 V output voltage.

The Output Voltage (V)	Inter-Bridge Phase-Shift Angle φ_{AD} (rad)	Intra-Bridge Phase-Shift Angle φ_{AB} (rad)
50	2.094	4.002
60	1.683	3.352
70	1.516	3.789
80	1.612	4.180
90	1.292	4.012
100	0.990	3.722

Table 4. Output voltage 100 V output power 100 W–200 W change optimal phase-shift angle combination table.

| Output Power (W)	Inter-Bridge Phase-Shift Angle φ_{AD} (rad)	Intra-Bridge Phase-Shift Angle φ_{AB} (rad)
150	0.696	3.550
160	0.750	3.582
170	0.806	3.614
180	0.865	3.649
190	0.925	3.684
200	0.990	3.722

4. Experimental Verification

Using the parameters given in Table 5, a test prototype was built for experimental verification of the theoretical analysis.

Table 5. Main circuit parameters of the experimental prototype.

Parameter Name	Parameter Value
Input Voltage V_{in}	100 V
Output Voltage V_o	100 V
Switching Frequency f_s(Hz)	100 kHz
Transformer Ratio	1:1
Resonant Inductor	146 μH
Resonant Capacitor	24 nF
Rated Power	200 W
Dead Time	200 ns
MOSFET	20N60C3

During the experiments, several different sets of phase-shift angles were selected for the experiments. Due to the need to ensure the safety of the experiments during the design process, the output current quickly reached the current limit value when the combination of phase-shift angles with larger values of reactive power were selected, which also confirms that the larger the reactive power, the lower the system efficiency. Therefore, the selected combinations of phase-shift angles are near the reactive power minimum point.

Firstly, the combination of phase-shift angle of the system output was used in the experiment. When the combination of inter-bridge phase-shift angle φ_{AD} and intra-bridge phase-shift angle φ_{AB} was (57°, 213°), the soft-switching waveforms of bridge-arm A, bridge-arm B and bridge-arm C were obtained, as shown in Figures 33–35. In the figures, channel 1 is the driving voltage, channel 2 is the resonant current and channel 3 is the drain source voltage.
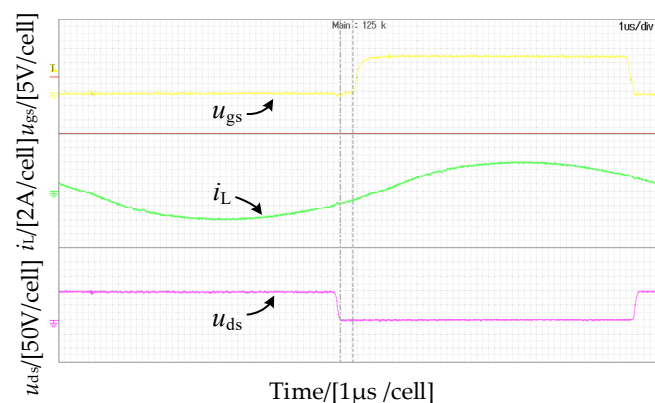
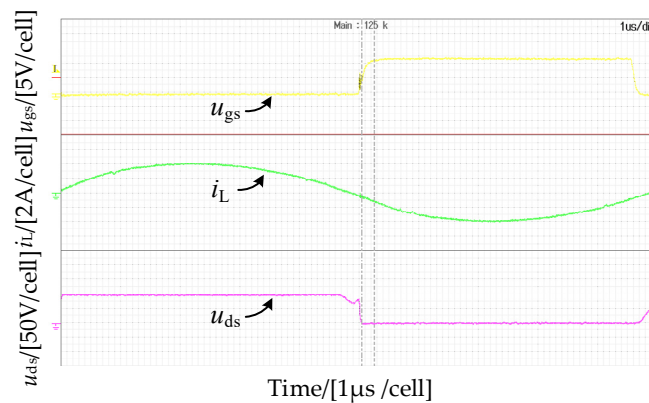**Figure 33.** Bridge-arm A soft-switching waveform diagram.

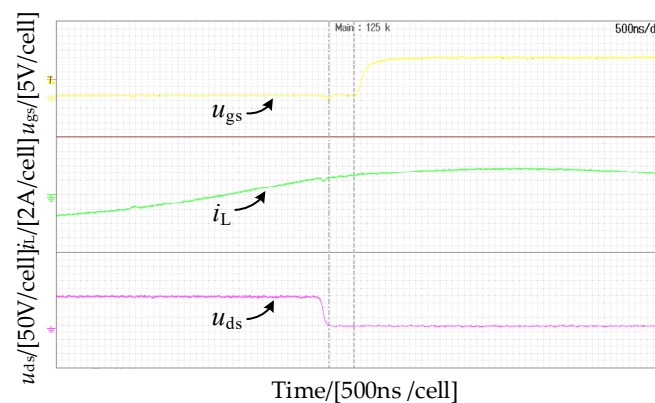**Figure 34.** Bridge-arm B soft-switching waveform diagram.

Figure 35. Bridge-arm C soft-switching waveform diagram.

The waveforms of reactive power and active power are shown in Figure 36, where channel 1 is the voltage u_{AB} waveform at the midpoint of the two bridge arms on the primary side, channel 2 is the resonant current waveform, channel 3 is the voltage u_{DC} waveform at the midpoint of the two bridge arms on the secondary side and channel 4 is the output current waveform.
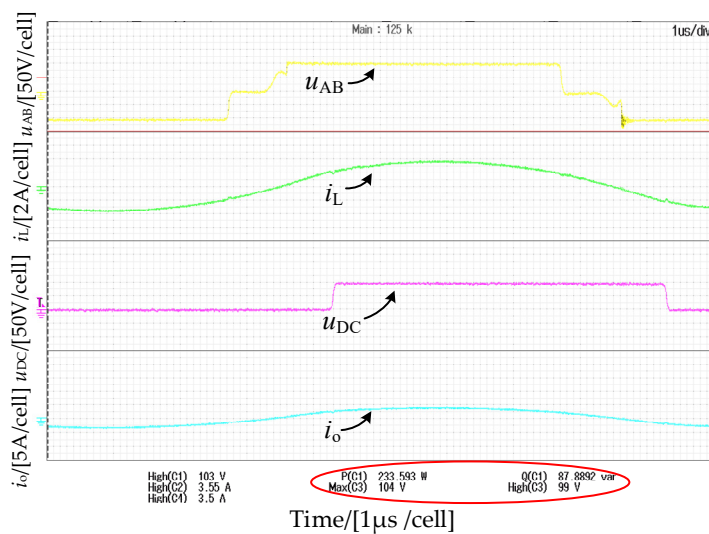

Figure 36. $\varphi_{AD} = 57°$ and $\varphi_{AB} = 213°$ experimental waveforms with reactive power optimization control.

It can be seen that the combination of the phase-shift angle of the output of the reactive power flow diagram is located near the soft-switching boundary of the B-bridge arm, but

the parasitic parameters of the switching device and transformer are not considered in the simulation. However, in the actual experimental process, the parasitic parameters of the PCB board and the switching device and other factors affect the circuit operation, resulting in the actual experimental results of the B-bridge arm not achieving soft-switching; in the actual simulation, because the transformer is the ideal case, the simulation of the B-bridge arm achieves ZVS soft switching, resulting in deviations between the theoretical simulation results and the actual experimental results.

When the combination of inter-bridge phase-shift angle φ_{AD} and intra-bridge phase-shift angle φ_{AB} is (40°, 171°) and the combination of inter-bridge phase-shift angle φ_{AD} and intra-bridge phase-shift angle φ_{AB} is (49°, 190°), the obtained active and reactive power waveforms are as shown in Figures 37 and 38.

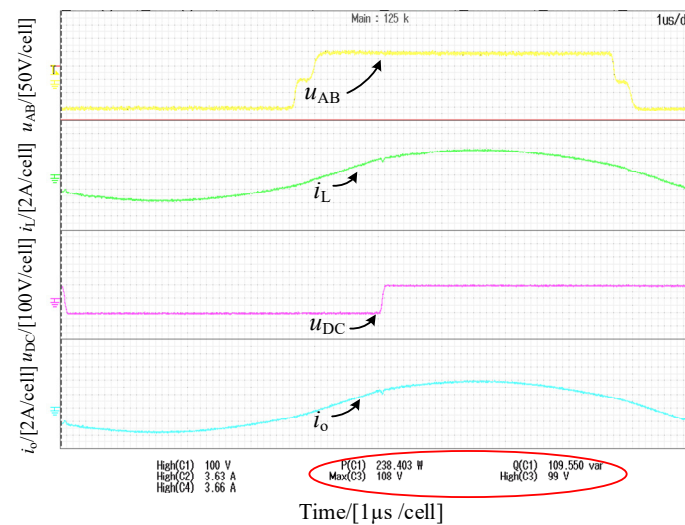**Figure 37.** φ_{AD} = 40° and φ_{AB} = 171° experimental waveforms without reactive power optimization.
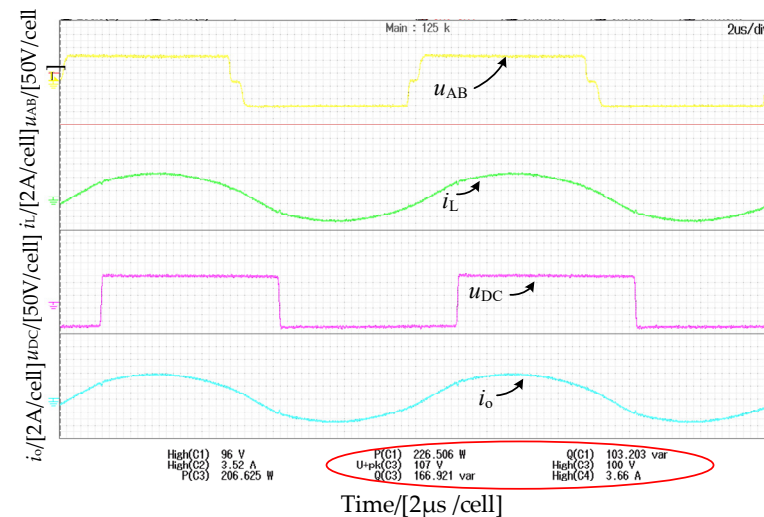

Figure 38. φ_{AD} = 49° and φ_{AB} = 190° experimental waveforms without reactive power optimization.

From the above experimental waveform diagram, it can be seen that the reactive power of the phase-shift angle combination output by the flow chart is smaller than the reactive power of the randomly selected phase-shift angle, and it can be learned from the calculated efficiency that the system efficiency is the highest for the phase-shift angle combination output by the flow chart. The transmission efficiencies of the three phase-shift angle combinations are calculated for an output power of 200 W, as shown in Table 6.

Table 6. Reactive power when the transmitted power is 200 W.

Output Power	Phase-Shift Angle Combination	Reactive Power Value
200 W	(57°, 213°)	86.8 Var
	(40°, 171°)	109.5 Var
	(49°, 190°)	103.2 Var

5. Conclusions

In this paper, a reactive power-minimization control strategy is proposed with the topology of series-resonant DAB, EPS is analytically selected as the modulation method and the reactive power of the system is reduced as the objective, with the realization of full-bridge arm ZVS as the premise. By analyzing and studying the objective function, the reactive power-minimization control algorithm is designed and the optimization flow chart is drawn, and the two cases of gain M less than and M equal to 1 are verified by simulation. The simulation results from Figures 31 and 32 show that when the gain $M = 0.6$, the reactive power value of the system output phase-shift angle combination is 10 Var smaller than the reactive power of the randomly selected phase-shift angle combination. The simulation results from Figures 26 and 30 show that when the gain $M = 0.8$, the reactive power value of the system output phase-shift angle combination is 11.7 Var smaller than the reactive power of the randomly selected phase-shift angle combination. The case of gain $M = 1$ was verified experimentally, and as can be seen from the data in Table 6, the reactive power values at the output of the system were reduced by 22.7 Var and 16.4 Var compared to two randomly chosen combinations of phase-shift angles. Therefore, it can be proved that the control strategy can effectively improve the system efficiency.

Author Contributions: Conceptualization, investigation, supervision, project administration and funding acquisition, J.W. and X.S. (Xiaofeng Sun); re-sources, methodology, software, validation and writing—original draft preparation, W.Z.; formal analysis and data curation, X.S. (Xinyu Su). All authors have read and agreed to the published version of the manuscript.

Institutional Review Board Statement: Not applicable.

Informed Consent Statement: Not applicable.

Data Availability Statement: Not applicable.

Conflicts of Interest: The authors declare no conflict of interest.

References

1. De Doncker, R.W.; Divan, D.M.; Kheraluwala, M.H. A three-phase soft-switched high-power-density DC/DC converter for high-power applications. *IEEE Trans. Ind. Appl.* **1991**, *27*, 63–73. [CrossRef]
2. Zhao, B.; Song, Q.; Liu, W.; Sun, Y. Dead-Time Effect of the High-Frequency Isolated Bidirectional Full-Bridge DC–DC Converter: Comprehensive Theoretical Analysis and Experimental Verification. *IEEE Trans. Power Electron.* **2014**, *29*, 1667–1680. [CrossRef]
3. Zhao, B.; Yu, Q.; Sun, W. Extended-Phase-Shift Control of Isolated Bidirectional DC–DC Converter for Power Distribution in Microgrid. *IEEE Trans. Power Electron.* **2012**, *27*, 4667–4680. [CrossRef]
4. Verma, V.; Gupta, A. Performance enhancement of the Dual Active Bridge with dual phase shift control and variable frequency modulation. In Proceedings of the IEEE International Conference on Power Electronics, Drives and Energy Systems, Trivandrum, India, 14–17 December 2016; pp. 1–6.
5. Zhao, B.; Song, Q.; Liu, W.; Sun, Y. Overview of Dual-Active-Bridge Isolated Bidirectional DC-DC Converter for High-Frequency-Link Power-Conversion System. *IEEE Trans. Power Electron.* **2014**, *29*, 4091–4106. [CrossRef]
6. Zhao, B.; Yu, Q.; Sun, W. Bi-directional Full-bridge DC-DC Converters With Dual-phase-shifting Control and Its Backflow Power Characteristic Analysis. *Proc. CSEE* **2012**, *32*, 43–50.
7. Shi, Y.; Li, R.; Xue, Y.; Li, H. Optimized Operation of Current-Fed Dual Active Bridge DC–DC Converter for PV Applications. *IEEE Trans. Ind. Electron.* **2015**, *62*, 6986–6995. [CrossRef]

8. Han, W.; Ma, R.; Liu, Q.; Corradini, L. A conduction losses optimization strategy for DAB converters in wide voltage range. In Proceedings of the IECON 2016—42nd Annual Conference of the IEEE Industrial Electronics Society, Florence, Italy, 23–26 October 2016; pp. 2445–2451.

9. Sun, X.; Wang, H.; Qi, L.; Liu, F. Research on Single Stage High Frequency Link SST Topology and Its Optimization Control. *IEEE Trans. Power Electron.* **2020**, *35*, 8701–8711. [CrossRef]

10. Wen, H.; Chen, J. Control and efficiency optimization of Dual-Active-Bridge DC/DC converter. In Proceedings of the 2016 IEEE International Conference on Power Electronics, Drives and Energy Systems (PEDES), Trivandrum, India, 14–17 December 2016; pp. 1–6.

11. Liu, B.; Davari, P.; Blaabjerg, F. An Optimized Control Scheme to Reduce the Backflow Power and Peak Current in Dual Active Bridge Converters. In Proceedings of the 2019 IEEE Applied Power Electronics Conference and Exposition (APEC), Anaheim, CA, USA, 17–21 March 2019; pp. 1622–1628.

12. Bai, H.; Mi, C. Eliminate Reactive Power and Increase System Efficiency of Isolated Bidirectional Dual-Active-Bridge DC-DC Converters Using Novel Dual-Phase-Shift Control. *IEEE Trans. Power Electron.* **2008**, *23*, 2905–2914. [CrossRef]

13. Wen, H.; Xiao, W.; Su, B. Nonactive Power Loss Minimization in a Bidirectional Isolated DC–DC Converter for Distributed Power Systems. *IEEE Trans. Ind. Electron.* **2014**, *61*, 6822–6831. [CrossRef]

14. Shi, H.; Wen, H.; Chen, J.; Hu, Y.; Jiang, L.; Chen, G. Minimum-Reactive-Power Scheme of Dual Active Bridge DC-DC Converter With 3-Level Modulated Phase-Shift Control. *IEEE Trans. Ind. Appl.* **2017**, *53*, 5573–5586. [CrossRef]

15. Tong, A.; Hang, L.; Li, G.; Jiang, X.; Gao, S. Modeling and Analysis of a Dual-Active-Bridge-Isolated Bidirectional DC-DC Converter to Minimize RMS Current With Whole Operating Range. *IEEE Trans. Power Electron.* **2018**, *33*, 5302–5316. [CrossRef]

16. Li, X.; Bhat, A.K.S. Analysis and Design of High-Frequency Isolated Dual-Bridge Series Resonant DC/DC Converter. *IEEE Trans. Power Electron.* **2010**, *25*, 850–862.